Available online at www.sciencedirect.com

ScienceDirect

Geochimica et Cosmochimica Acta 334 (2022) 1–13

Geochimica et Cosmochimica Acta

www.elsevier.com/locate/gca

New constraints on the abundances of phosphorus and sulfur in the lunar core: High-pressure and high-temperature experimental study of the Fe—S—P ternary system

Kuan Zhai [a,b], Yuan Yin [c,*], Shuangmeng Zhai [a,*]

[a] *Key Laboratory of High-temperature and High-pressure Study of the Earth's Interior, Institute of Geochemistry, Chinese Academy of Sciences, Guiyang 550081 China*

[b] *University of Chinese Academy of Sciences, Beijing 100049, China*

[c] *State Key Laboratory of Ore Deposit Geochemistry, Institute of Geochemistry, Chinese Academy of Sciences, Guiyang 550081, China*

Received 5 February 2022; accepted in revised form 22 July 2022; available online 29 July 2022

Abstract

High-pressure and high-temperature experiments for the Fe—S—P ternary system were performed at 3–5 GPa and 1173–1873 K. We systematically investigated the effect of pressure, temperature, and bulk composition on the phase relationships, on the core crystallization sequences, and on the presence of sulfur and phosphorous in the lunar core. Our experimental results indicate that while up to < 1 wt% phosphorus can be dissolved in solid iron in the Fe—S—P ternary system at 3 and 5 GPa, S dissolution in solid iron is near negligible. On the iron rich (S + P < 10 wt%) side of the Fe—S—P phase diagram completely miscible Fe—S—P liquids were observed. Combined with previous experimental results, the relationship of the sulfur content in the liquid metal (X_S^{liquid}) and the partitioning coefficient of phosphorus (D_P) between the solid and liquid metal follows an equation of $lgD_P = -1.8286 - 17.87 \times lg\left(1 - X_S^{liquid}\right)$. Tradeoff between the liquidus of the Fe—S—P system and the (S + P) content of the lunar core well constrain the upper limit of the (S + P) content in the liquid lunar outer core to the concentrations between 8.7 and 13.1 wt%. Using the result of the phosphorus coefficient and our partitioning model, we further assessed the abundances of 6.08–7.15 wt% S, 0.54 ± 0.01 wt% P in the lunar liquid outer core, and 0.05 ± 0.01 wt% S, 0.07 ± 0.01 wt% P in the lunar solid inner core, respectively. Integrating the observed lunar core adiabat and the pressure dependence of the Fe—S—P liquidus temperature, we propose that the solidification regime in the lunar core will switch from bottom-up to top-down once the abundance of (S + P) in the liquid outer core exceeds 3.5 wt% as the core evolves.

Keywords: Lunar core; Fe—S—P; Phase diagram; Partitioning coefficient; Inner core solidification

1. INTRODUCTION

Geophysical and geochemical observations suggest that the moon may have a small, at least partially molten, Fe-rich metallic core (Matsuyama et al., 2016; Rai and van Westrenen, 2014; Righter, 2002; Weber et al., 2011) while an ancient lunar core dynamo sustained a global magnetic field until ~ 1.92–0.80 Ga ago (Mighani et al., 2020). To sustain the composition convection in an Fe-rich lunar core, one or more light elements (such as S and C) would be required to produce sufficient compositional buoyancy (Laneuville et al., 2014). S and P commonly found alloyed with Fe-Ni in iron meteorites (Teplyakova, 2011), regarded as fragments of the cores of differentiated planetesimals, also implies the presence of light elements as a general feature in planetary cores.

* Corresponding authors at: Institute of Geochemistry, Chinese Academy of Sciences, Guiyang 550081, China.

E-mail addresses: yinyuan@mail.gyig.ac.cn (Y. Yin), zhaishuangmeng@mail.gyig.ac.cn (S. Zhai).

https://doi.org/10.1016/j.gca.2022.07.024

0016-7037/

In addition to carbon, the relatively high abundances for sulfur predicted for BSE compared to other light element, and its high solubility in liquid iron and its ability to reduce the core's density, velocity, electrical conductivity, and liquidus temperature, sulfur is probably a dominant light element in the lunar core (Jing et al., 2014; Pommier, 2018; Weber et al., 2011). Many studies have investigated the abundance of sulfur in the lunar core from geochemical (Rai and van Westrenen, 2014; Righter et al., 2017; Steenstra et al., 2016; Steenstra et al., 2017a) and geophysical models (Antonangeli et al., 2015; Jing et al., 2014; Kuskov and Belashchenko, 2016; Weber et al., 2011). But the sulfur abundance in the primordial lunar core remains debatable. Through a mass balance model, the partition coefficient of sulfur (~0.25–1.30) and the sulfur concentration in bulk silicate Moon (BSM) (74.5 ± 4.5 ppm), 0.16 wt % sulfur is predicted to reside in the lunar core (Steenstra et al., 2017a). Ding et al (2018) estimated a higher sulfur abundance up to 120 ppm in BSM through experiments on sulfur content at sulfide saturation of lunar magmas with high and intermediate TiO_2 contents. In this case, the sulfur content in the lunar core is less than 0.24 wt% estimated by a core-mantle differentiation model from Steenstra et al (2017a). Differently, metal/silicate partition models for siderophile elements provide strong geochemical support for the presence of a deep lunar magma ocean and a significant amount of S (6 wt%) in the lunar core (Rai and van Westrenen, 2014). Steenstra et al. (2016) suggested that only a fully molten lunar core contains more than 8 wt% S could stratify lunar mantle depletions when the mantle temperature between the solidus and liquidus. On the other hand, a significant amount of sulfur is expected to reside in the lunar core when inferred from geophysical models, over an order of magnitude higher than cosmochemical estimations. Based on thermochemical evolution models, Laneuville et al. (2013) suggested that ~ 3 wt% S was necessary to solidify a 240 km radius lunar inner core, whereas Zhang et al. (2013) proposed that the lunar core's S content is ~ 5–10 wt%. Laneuville et al. (2014) further proposed an initial sulfur content of 7 ± 1 wt% in the core, or more than 12 wt% if the Moon never has an inner core. According to the sound velocity and density of Fe and Fe-S alloys measured experimentally, Jing et al. (2014) estimated 4 ± 3 wt% sulfur in the lunar outer core. Antonangeli et al. (2015) suggested that the lunar liquid outer core has 6–11 wt% sulfur. An experimental study of a multicomponent Fe-Ni—S—C system under lunar core conditions implies that an S- and C-poor core is sufficient to provide a heat source for the lunar core dynamo (Righter et al., 2017). Based on a comparison between previously published lunar composition models and molecular-dynamic calculation results, Kuskov et al. (2019) estimated that an Fe-S lunar core has a mean density of 7.1 g/cm^3 and a sulfur content of 3.5–6.0 wt%. The uncertainties in the lunar core size and density, the amount and nature of the light elements in the lunar core are still in doubt.

Another possible light element in the lunar core is phosphorus. As phosphorus abundance in the BSM is depleted relative to CI chondrites, phosphorus enrichment in the lunar core should arise from core-mantle differentiation (Righter, 2002; Righter and Drake, 1996). Previous estimations of the phosphorus abundance in the bulk silicate Moon and bulk Moon were approximately 20 ppm and 43 ppm, respectively, which yield ~ 0.1 wt% P content in the lunar core (O'Neill, 1991). Assuming the bulk Moon has a similar composition to bulk silicate Earth, Yin et al. (2019) estimated a slightly higher lunar core phosphorus content of 0.3 wt%. Though the geochemical and cosmochemical observations prefer a lunar core with < 0.5 wt% (S + P), the abundances of sulfur and phosphorus in the lunar core remains limited by the S and P budgets and pressure–temperature conditions in the primordial Moon.

Many works have studied sulfur or phosphorus partitioning between metal and silicate melts under the lunar core conditions (Righter 2019; Steenstra et al., 2017b), but no study investigates the abundances of sulfur and phosphorus from the aspect of the Fe—S—P system. Although the Fe—S—P system has a liquid immiscibility field at ambient pressure (Raghavan, 1988), complete miscibility between Fe-S and Fe-P liquids was observed at 23 GPa (Stewart and Schmidt, 2007). Determining the Fe—S—P phase diagram under lunar core conditions becomes vital to investigate the chemical state of sulfur and phosphorus in the lunar core. Experimental studies of the Fe—S—P ternary system under lunar core conditions are rare but necessary. A series of high-pressure and high-temperature (*P-T*) experiments were performed in this study to investigate the phase relationships, the melting temperatures, and the partitioning of phosphorus and sulfur between solid and liquid metals in the Fe—S—P system. These results were then used to constrain and discuss the compositional difference and the density deficit at the lunar inner-core boundary (ICB). Based on the new phase diagrams of the Fe—S—P system under high *P-T* conditions, we also propose a new solidification scheme for the lunar core.

2. MATERIALS AND METHODS

2.1. Starting materials

The starting materials investigated include Fe-2 wt% S-8 wt% P (Fe2S8P), Fe-4 wt% S-6 wt% P (Fe4S6P), Fe-5 wt % S-5 wt% P (Fe5S5P), Fe-6 wt% S-4 wt% P (Fe6S4P), Fe-8 wt% S-2 wt% P (Fe8S2P), Fe-2 wt% S-4 wt% P (Fe2S4P), and Fe-4 wt% S-2 wt% P (Fe4S2P). The Fe—S—P mixtures were prepared from pure Fe (99.9 % powder, Alfa Aesar), S (99.5 % powder, Alfa Aesar), and Fe_2P (99.5 % powder, Sigma-Aldrich). The mixtures were first homogenized by grinding under ethanol in an agate mortar for 1 h and then were dried at 383 K in a vacuum oven for 5 min. Subsequently, the starting materials were stored in a sealed glass container in a vacuum oven to avoid oxidation.

2.2. High-pressure and high-temperature experiments

Experiments at 3 GPa were conducted in a YJ-3000 t cubic press, where the pressure was generated by compressing pyrophyllite cubes (Fig. 1a). Graphite sleeve were used as heaters. An alumina sleeve was placed between the hea-

ter and the pyrophyllite as a thermal insulator. Seven starting materials were encapsulated in a hexagonal boron nitride (hBN) sample chamber with seven predrilled holes (Fig. 1a). Before the high-pressure experiments, the pyrophyllite cubes and plugs, the alumina sleeves, and the hBN capsules were preheated at 1073 K for 1 h to remove absorbed water. The pressure calibrations of this system have been described by Shan et al. (2007). The pressure uncertainty is ± 0.1GPa. A $W_{95}Re_5$-$W_{74}Re_{26}$ thermocouple was placed close to the sample to monitor the temperature, with an uncertainty of ± 25 K. No corrections were applied for the pressure effect on the thermocouple emf.

Experiments at 5 GPa were performed in a 1000-ton Kawai-type multi-anvil apparatus using an 18/11 assembly (Fig. 1b), consisting of a 5 wt% Cr_2O_3-doped MgO octahedron, a ZrO_2 thermal insulation sleeve, a straight-walled graphite furnace, and an hBN capsule. Pressure calibration was carried out based on the phase transitions of bismuth and SiO_2 (Bean et al., 1986; Bohlen and Boettcher, 1982). The uncertainty for the pressure is ± 0.5 GPa. Two hBN sample chambers filled with starting materials were symmetrically placed in the center of assembly (Fig. 1b), reducing the necessary experimental runs. The temperature was measured using a $W_{95}Re_5$-$W_{74}Re_{26}$ thermocouple inserted axially between the two sample chambers, the temperature uncertainty is about ± 5 K below 1000 K and ± 20 K at 1000–1900 K (Yin et al., 2022).

During the experiments, assemblies were first pressed to the desired pressure, 3 or 5 GPa, heated to 1173–1873 K at a constant rate of 50 K/min, and then held at the target temperature. Commonly, equilibrium can be achieved within several hours in a liquid state for Fe-P and Fe-S systems (Buono and Walker, 2011; Stewart and Schmidt, 2007; Yin et al., 2019). To ensure complete equilibration in the Fe—S—P system during the experiments, we set the heating time to be between 6 and 24 h. After this heating stage, the samples were rapidly quenched to room temperature by shutting down the power. All the recovered samples were then mounted in epoxy resin and polished to the mid-axis vertically with diamond suspending liquid for electron microprobe analyses. The backscattered electron (BSE) images and chemical composition analysis for run products were obtained with a JEOL JXA-8530F field emission electron probe, using a beam current of 10nA and 20 kV voltage with conventional ZAF data reduction techniques. The standards used for iron, sulfur, and phosphorus are Fe metal, pyrite, and apatite, respectively. We used a defocused 10–20 μm beam and a focused 1 μm probe beam to analyse the chemical composition of the liquids and solids, respectively.

3. RESULTS

The experimental conditions, observed phase assemblages and chemical compositions are summarized in Table S1. The EDXS results indicate a negligible amount of B, N and O dissolved in Fe—S—P melt. In fact, in a previous study of our group on the Fe-P binary system in the same sample assembly using the hBN capsule (Yin et al., 2019), the chemical composition analyses of the recovered Fe-P samples show that a negligible content of B, N, and O was detected. Some representative textures in the recovered samples are presented in Fig. 2.

3.1. Miscibility in Fe—S—P melts

In all recovered samples, we did not see any distinct immiscibility in the quenched melts. Backscattered electron images of some quenched samples show a similar dendritic growth texture (Fig. 2b-e, 2 g-i) to those observed by Stewart and Schmidt (2007). All melts contain < 8 wt% of phosphorus and < 25 wt% of sulfur (Table S1). In particular, the equilibrium melt in some runs exceeded the eutectic composition of the Fe-S and Fe-P binary systems. The content of (S + P) in the melts was generally less than the Fe-S eutectic composition of ~ 25 wt%. The shaded region in Fig. 3 indicates the predicted location of the field containing one solid and one liquid phase under pressure up to 23 GPa.

3.2. Fe—S—P phase diagrams at 3 and 5 GPa

A mineral phase assemblage of iron, phosphide (Fe_3P), and sulfide (FeS) with obvious grain boundary was

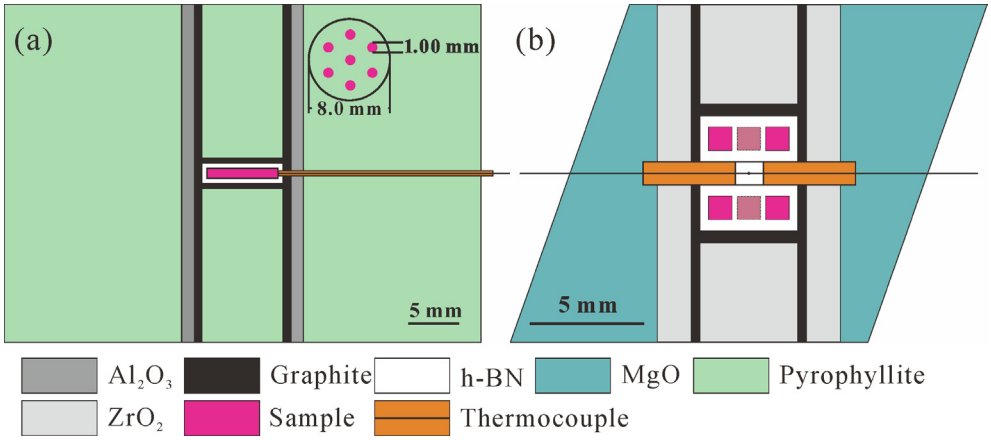

Fig. 1. Sketch of two assemblies. (a) and (b) show the cross-sections of the sample assemblies used in our experiments conducted at 3 and 5 GPa, respectively.

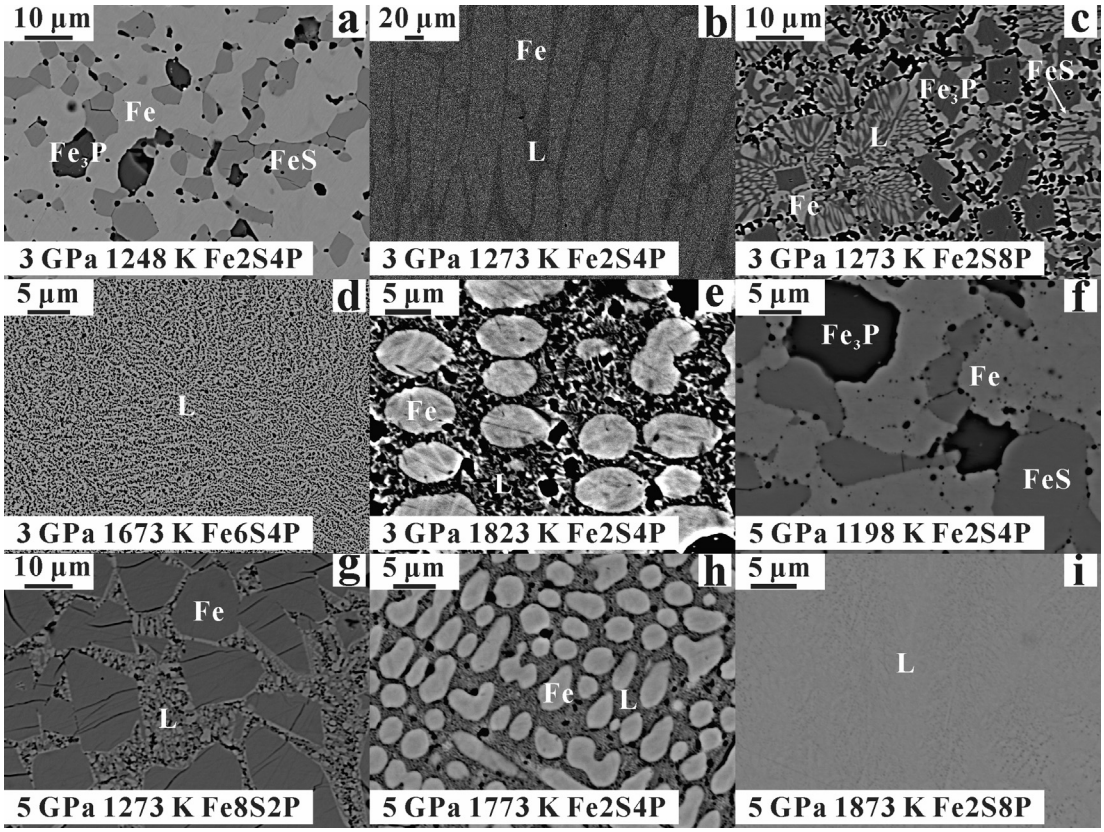

Fig. 2. Representative BSE images of run products in the Fe—S—P system under different pressures. (a) and (f) show typical textures of subsolidus phase assemblages. (b)-(e) and (g)-(i) indicate the quenched phase structures. The small black parts disseminated in (e), (f) and (h) are holes created during polishing.

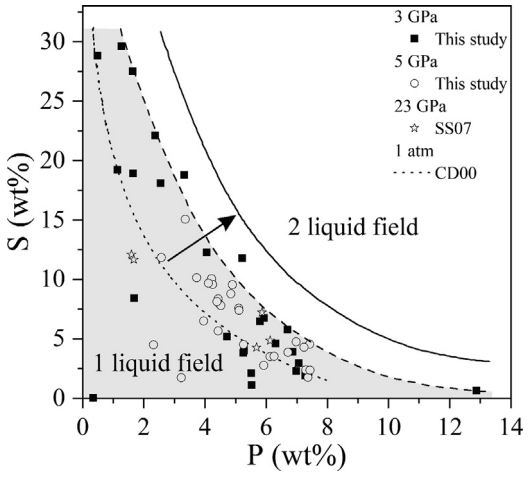

Fig. 3. The boundary of one-liquid and two-liquid fields range from 1173 to 1873 K up to 5 GPa. The dashed line is the lower limit of the boundary between the one-liquid field and two-liquid field suggested by the experimental results of 3–5 GPa from this study and at 23 GPa (Stewart and Schmidt, 2007). The dotted line is the estimated boundary at ambient pressure by Chabot and Drake (2000). The one-liquid field will extend with increasing pressure, and the real boundary may be located in the S—P—bearing area (solid line). SS07: Stewart and Schmidt (2007); CD00: Chabot and Drake (2000).

observed at temperatures lower than 1273 K at 3 GPa (Fig. 2a) for all the starting materials shown in Table S1. The Fe—S—P liquid appears until the temperature reached 1273 K at 3 GPa from low to high temperature, and phosphide and sulfide were only observed in run FSP-2 with Fe2S8P as the starting material. We estimate a eutectic temperature of 1261 K for the Fe—S—P system at 3 GPa. In the case of the iron-rich (6 wt% light element) experiments, solid iron reaches equilibrium with the melts at 3 GPa and up to 1823 K (Fig. 2e), while the S- or P-rich sample (10 wt% light element) was completely molten above 1673 K at 3 GPa (Fig. 2d), indicating a temperature above liquidus. The chemical composition of the melts above liquidus nearly approaches the chemical composition of the starting materials (10 wt% light element) in some runs performed over 1673 K. The same phase assemblage of Fe + Fe_3P + FeS (Fig. 2f) was observed at 5 GPa and 1198 K, and melts appeared above 1273 K (Fig. 2g). We estimated a eutectic temperature of 1234 K for the Fe—S—P system at 5 GPa, which is similar to that of the Fe-S system at 5.1 GPa of 1237 K (Liu and Li, 2020). All the S- or P-rich samples (10 wt% light element) completely melted above 1673 K (Fig. 2i), and the solids coexisted with melts in all the iron-rich (6 wt% light element) samples under conditions above the eutectic temperature and 5 GPa (Fig. 2h).

The fully molten and nonmelted samples constrain the lower bounds on the liquidus curve and the upper bounds on the solidus curve, respectively (Fig. 4a, 4b). No phase transition of Fe_3P was observed below 8 GPa and at room temperature (Lai et al., 2020; Scott et al., 2007). Stewart and Schmidt (2007) reported different solid-phase assemblages due to a change in the stability of sulfide with pressure as FeS transforms into Fe_3S_2 under 14–18 GPa, and further into Fe_3S under 18–23.5 GPa (Li and Fei, 2014). Phase diagrams indicate that α-Fe (body-center cubic structure, bcc) transforms to γ-Fe (face-center cubic structure, fcc) at 1065 K at 3 GPa and 985 K at 5 GPa, to δ-Fe (body-center cubic structure, bcc) at 1840 K at 3 GPa, and to a liquid at 1905 K at 3 GPa and 1973 K at 5 GPa (Liu and Bassett, 1975). Thus, there are two structures of iron, α- and γ-Fe, under our experimental conditions. γ-Fe is usually not quenchable, so the iron in all quench samples is α-Fe in the bcc structure.

Results on binary Fe-P (Minin et al., 2019; Yin et al., 2019) and Fe-S (Brett and Bell, 1969; Liu and Li, 2020) systems were combined with our Fe—S—P melt experiments to construct isothermal sections of the Fe—S—P ternary phase diagram at 3–5 GPa (Fig. 4c). These isothermal sections show that the solubility of phosphorus and sulfur in liquids decreases with increasing temperature and pressure (Fig. 4c) since the liquid composition moves toward the iron end member with increasing temperature and pressure, which is consistent with the results of Stewart and Schmidt (2007).

4. DISCUSSION

4.1. The occurrence of miscible Fe—S—P melt

Most Fe-light element (e.g., S, Si, C, and O) ternary systems exhibit a liquid miscibility gap under ambient pressure (Raghavan, 1988). Metallurgical data at atmospheric pressure (Wang et al., 1991) and high-pressure data up to 7.7 GPa (Dasgupta et al., 2009; Corgne et al., 2008) in the Fe—S—C system suggest that the interaction between

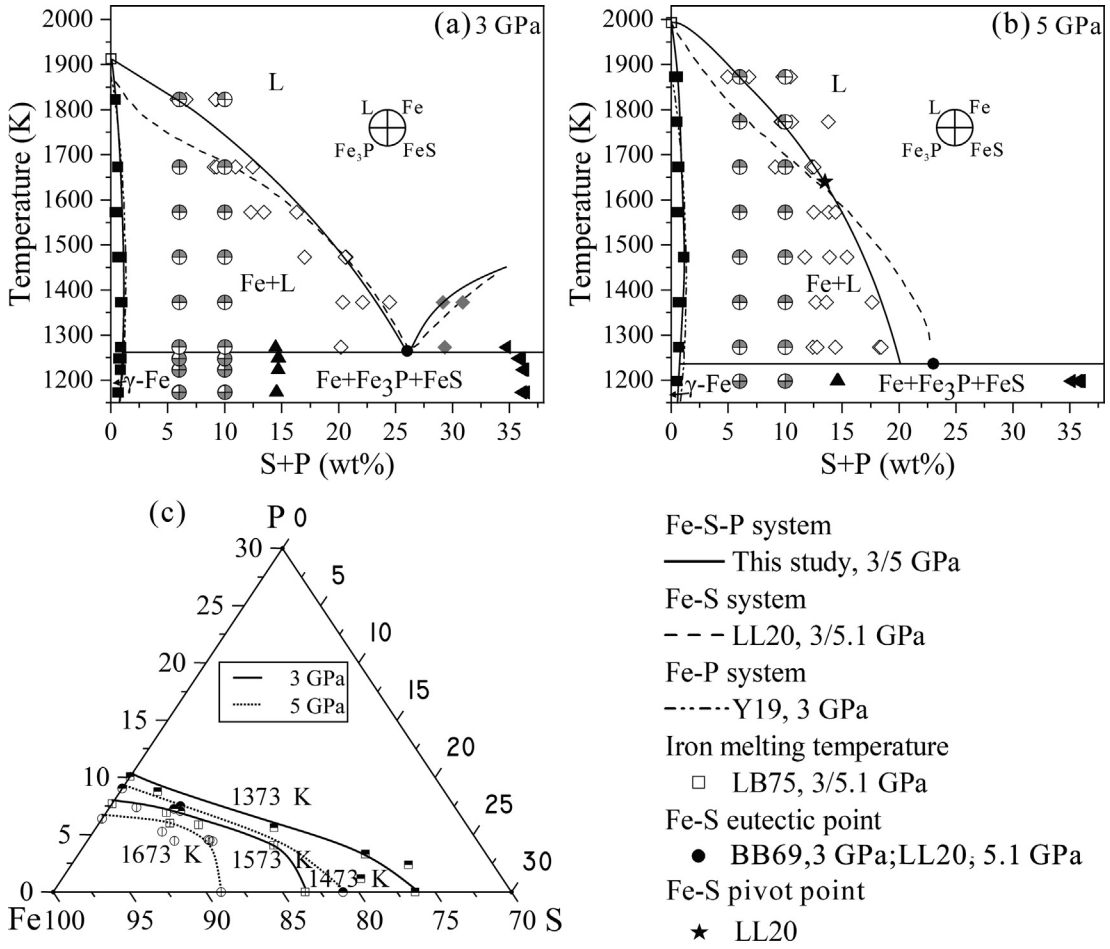

Fig. 4. Phase diagrams of Fe—S—P system. (a) and (b) represent the temperature-composition (X_{P+S}, wt%) relationships at 3 and 5 GPa, respectively. (c) is an isothermal section of an iron-rich portion of the Fe—S—P system. The liquidus surface of the ternary material in diagrams (a) and (b) demonstrates the cotectic relationship between the Fe-S and Fe-P binary eutectic points. Open square is the pure iron melting temperature taken from Liu and Bassett (1975). Solid triangle is Fe_3P or FeS compound. In picture, a and b, the open diamonds and black squares represent the total of sulfur and phosphorus in the melts and solid iron, respectively. The star in diagram (b) is the pivot point in the Fe-S system. BB69: Brett and Bell (1969); LB75: Liu and Bassett (1975); LL20: Liu and Li (2020); Y19: Yin et al. (2019).

C and S produce S-rich and C-rich immiscible melts at sufficiently high S and C content. The solubility of C in liquid Fe decreases modestly with increasing sulfur content, indicating the sulfur atom is easier to form ionic bond with Fe atom than C atom, and the C atom will find it difficult to replace attractive Fe-S bonds with repulsive Fe-C bonds (Sahajwalla and Khanna, 2003). The miscibility gap also was observed in Fe-S-Si system, Fe and S control the evolution of the miscibility gap, more than Si or C (Morard and Katsura, 2010, and reference therein). It must be note that the Fe-Si-C ternary system is completely miscible (Siebert et al., 2005). The mutual solubility of light elements (S, Si, C, and O) is enhanced with increasing pressure and the closure acceleration of miscibility gap could be linked with pressure because of the increasing structural similarity of the immiscibile melts that evolves as the pressure increases (Deng et al., 2013; Sahajwalla and Khanna, 2003).

Chabot and Drake (2000) determined the location of the liquid immiscibility field of the Fe—S—P system at 1 atmosphere by integrating a published Fe—S—P phase diagram (Raghavan, 1988) and solid-metal-liquid–metal partition experiments (Jones and Drake, 1983; Malvin et al., 1986). Malvin et al. (1986) noted that different starting compositions in the Fe-Ni—S—P system do not produce two immiscible liquids at high-temperatures when the oxygen fugacity is near IW, but that liquid immiscibility occurs when the environment is much more reducing. A miscibility Fe—S—P melts was observed due to the similarity structure of Fe-S and Fe-P melts and insufficient S in Fe—S—P bulk composition. Since we did not see any immiscibility of the Fe—S—P melts in this study, the shaded region in Fig. 3 only indicates a potential lower boundary of the liquid immiscibility field. The accurate border of the immiscibility field in the Fe—S—P system on the iron-rich side may shift towards an S—P—rich region with increasing pressure.

4.2. Pressure effect on Fe—S—P eutectic composition and eutectic temperature

Phosphorus solubility in solid iron in the Fe—S—P system at 3 and 5 GPa is < 1 wt%, while sulfur solubility is generally < 0.1 wt%, indicating that nearly all the sulfur goes into liquid in these systems (Table S1). The sulfur content in the melt decreases with increasing temperature (Fig. 4). The eutectic liquid contains approximately 26.5 wt% (S + P) at 3 GPa and $\sim$ 20 wt% (S + P) at 5 GPa, indicating that the solubility of sulfur and phosphorus in the eutectic liquid decreases with increasing pressure. The eutectic composition of the Fe—S—P system at 3 GPa is consistent with Brett and Bell (1969), suggesting a negligible impact of phosphorus at 3 GPa. But the eutectic composition at 5 GPa is $\sim$ 20 wt% (S + P) in the Fe—S—P system, which is lower than that of $\sim$ 22 wt% S in the Fe-S system (Table 1, Liu and Li, 2020), suggesting that the phosphorus impact on the eutectic composition becomes significant with increasing pressure. The eutectic composition of the Fe—S—P system migrates towards the Fe-rich side with increasing pressure which is consistent with the Fe-S system (Buono and Walker, 2011). According to previous studies, the liquidus curve passes through a pivot point at 13.5 wt % S and 1640 K for the Fe-S system from pressure of 1 bar to 10 GPa (Buono and Walker, 2011, Liu and Li, 2020). A pivot point represents an equilibrium of liquid and crystalline metals that allows pressure to vary considerably without impacting the melting behavior. Compared to the Fe-S liquidus curve at 5.1 GPa, the Fe—S—P liquidus curve is the same as for the Fe-S system before the pivot point but becomes steeper at higher (S + P) contents (Fig. 4b). This variation is most likely due to the join of phosphorus.

The eutectic temperature of the Fe-S system remains roughly constant up to 6 GPa (Buono and Walker, 2011) and eventually increases with increasing pressures above 21 GPa, as shown in Fig. 5 and listed in Table 1 (Li and Fei, 2014). Our observed miscibility of the Fe—S—P liquid also supports the idea that the eutectic temperature does not change significantly up to 5 GPa. Although Stewart and Schmidt (2007) carried out high-pressure experiments at 23 GPa for the Fe—S—P system, they did not accurately determine the eutectic temperature. Similar to the Fe-S binary system, we suggest that the eutectic temperature of the Fe—S—P system may remain constant in the low-pressure range, decrease at 6–14 GPa, and increase at 14–23.5 GPa (black dotted line in Fig. 5). The solidus temperature of the Fe—S—P ternary system ($\sim$1261 K at 3 GPa, $\sim$1234 K at 5 GPa) is lower than those of the Fe-C and Fe-P binary systems but is close to the Fe-S binary system under the same pressure (Table 1). Therefore, the eutectic temperature of the iron-rich Fe—S—P system is determined by sulfur rather than by phosphorus.

4.3. Phosphorus partition coefficients between solid and liquid metals

The partition coefficient defines how elements are distributed between two equilibrium phases. The Nernst solid–liquid partition coefficient D for element i between two coexisting phases is calculated as follows:

$$D_i^{solid/liquid} = \frac{C_i^{solid}}{C_i^{liquid}} \quad (1)$$

where C is the concentration, in wt%, of element i in either the solid metal or melts (Wade and Wood, 2005). The sulfur solubility in solid Fe is negligible ($<$0.1 wt%, Table S1), and thus we only considered the partition of phosphorus between the solid and liquid metals here.

In order to compare the phosphorus partition coefficient more intuitively with the Fe-P system at 3 GPa (Yin et al., 2019) and the Fe—S—P system at 23 GPa (Stewart and Schmidt, 2007), we calculated the phosphorus partition coefficients (D_P) at 3 and 5 GPa (Fig. 6a) based on the phosphorus content in the residual solid iron and melts in the recovered samples of Fe2S4P. The D_P value increases with increasing pressure (Fig. 6a). At the conditions relevant to the lunar core (4.5–5.3 GPa, Garcia et al., 2011; Kuskov and Kronrod, 1998; 1773–1973 K, Chacko and De Bremaecker, 1982; Laneuville et al., 2014; Zhang et al., 2019), the D_P value was estimated as being 0.13 $\pm$ 0.03 according to our partitioning model. Righter and Drake (2000) indicated a relationship between

Table 1
Eutectic/cotectic temperature and composition of iron alloy at different pressures.

System	Eutectic/Cotectic Temperature (K)	Light elements (wt%)	Pressure (GPa)	Reference
Fe-C	1448	3.7	4.5	Hirayama et al., 1993
	1518	4.0	4.0	Fei and Brosh, 2014
Fe-S	1263	27.1	3.0	Brett and Bell, 1969
	1237	22.0	5.1	Liu and Li, 2020
Fe-P	1321	10.5	0.0001	Zaitsev et al., 1995
	1358	10.1	3.0	Yin et al., 2019
	1348	9.6	6.0	Minin et al., 2019
	1548	9.0	23.0	Stewart and Schmidt, 2007
Fe—S—P	1261	26.5	3.0	This study
	1234	20.0	5.0	This study

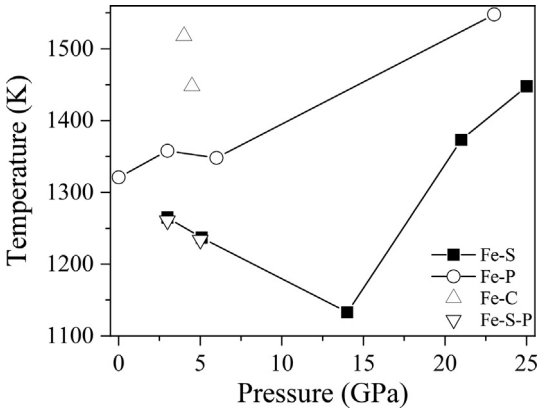

Fig. 5. The eutectic temperature of Fe-L (L = C, S, P) system varies with pressure. The Fe-C binary system at 4 GPa (Fei and Brosh, 2014), 4.5 GPa (Hirayama et al., 1993). The Fe-S binary system at 3 GPa (Brett and Bell, 1969), 5.1 GPa (Liu and Li, 2020), 14 GPa (Fei et al., 1997), 21 GPa (Fei et al., 2000) and 25 GPa (Li et al., 2001). The Fe-P binary system at 1 bar (Zaitsev et al., 1995), 3 GPa (Yin et al., 2019) and 6 GPa (Minin et al., 2019). The Fe—S—P ternary system at 3 and 5 GPa (this study).

D_P and sulfur content in the melt at 1 atmosphere: $\lg D_P = 7.03 \times (X_S)^2 - 1.05$, where X_S is the sulfur mole fraction. Thus, the D_P increases from 0.095 to 0.115 with sulfur-free to 8 wt% sulfur. At 23 GPa, D_P increases to 0.46 at 1573 K in the case of the sulfur-poor Fe—S—P ternary system (Stewart and Schmidt, 2007). Pressure affects the D_P value positively because the phosphorus solubility in solid iron increases with increasing pressure (Stewart and Schmidt, 2007; Yin et al., 2019).

The 'epsilon formalism' describes the effects of temperature, pressure and metal composition on the partitioning of trace elements between solid and liquid metals (Wade and Wood, 2005). Tao and Fei (2021) followed 'epsilon formalism' well parameterized the D_{Si} with X_S^{liquid}, and deduced the pressure and compositional difference at the Mercury's ICB. With this approach, D_P is parameterized as a function of pressure, temperature, and X_i (P and S contents):

$$lgD_P = a + b/T + cp/T + dlg\left(1 - X_S^{liquid}\right) + elg\left(1 - X_P^{liquid}\right) + flg\left(1 - X_P^{solid}\right) \quad (2)$$

where T is the temperature in K and p is the pressure in GPa. X_S^{liquid}, X_P^{liquid} and X_P^{solid} are the mole fractions of sulfur in the liquid and phosphorus in the liquid and the solid phases, respectively. The temperature dependences of trace element partition coefficients in Fe-(Ni)-S systems (Jones and Malvin, 1990) and carbon-saturated Fe—S—C systems (Hayden et al., 2011) are very weak. The activity coefficients of trace elements in solid Fe-Ni metal relative to the changes in liquid Fe-Ni metal are also small (Jones and Malvin, 1990). Without considering the effects of temperature and trace elements on solid metals, Jones and Malvin (1990) described well phosphorus and sulfur partitioning behavior in Fe-Ni-S, Fe-Ni-P, and Fe-Ni—S—P systems. Based on the 'epsilon formalism', we modeled the phosphorus partition coefficient D_P between the solid and liquid metals under pressures from 3 to 23 GPa using the data from this study and some previous studies (Stewart and Schmidt, 2007). Due to the negligible effect of T, X_P^{liquid} and X_P^{solid}, the parameters b and c and the last two items in equation (2) are equal to zero. The linearly corrected relation between lgD_P and $lg\left(1 - X_S^{liquid}\right)$ is plotted in Fig. 6b as:

$$lgD_P = -1.8286 - 17.87 \times lg\left(1 - X_S^{liquid}\right) \quad (3)$$

with $R^2 = 0.9569$.

As shown in Fig. 6c, we plotted the calculated D_P from Eq. (3) and the experimentally determined D_P from this study and previous studies (Stewart and Schmidt, 2007) and find a good agreement on these data. The experimental results of the Fe-Ni—S—P system suggest that there is no significant variation in partition coefficients with temperature and pressure for sulfur, and that the phosphorus partition coefficient shows a significant pressure effect (Stewart et al., 2009). No systematic variations in the phosphorus partition coefficient were observed in the Fe—S—P system (Stewart and Schmidt, 2007) and the Fe-Ni—S—P system (Stewart et al., 2009) at 23 GPa, indicating a small impact from nickel. Moreover, the partition coefficients of phosphorus in the Fe-Ni—S—P system fit well in our phosphorus partition model (Fig. 6c), suggesting that the partition coefficient values of the phosphorus and sulfur mole fraction in the melt in the Fe-Ni—S—P system can be roughly inferred from our phosphorus partition model.

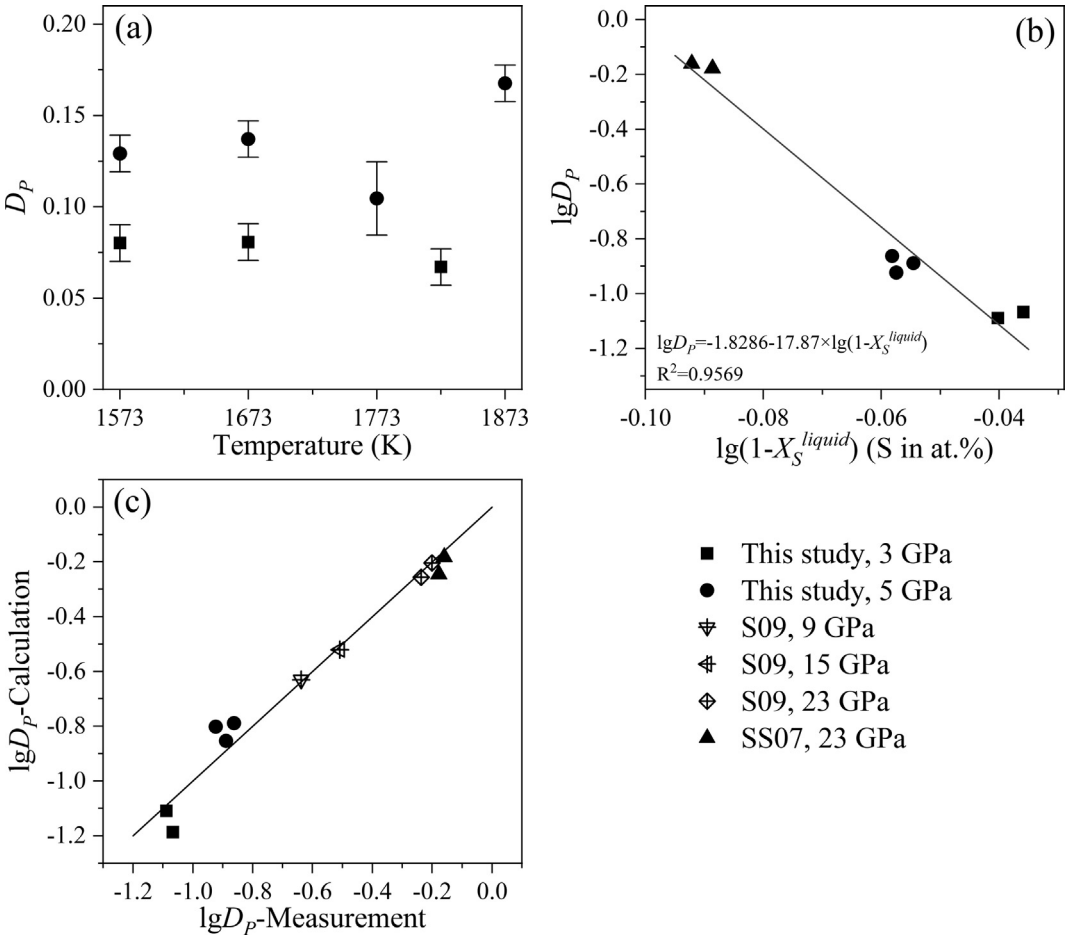

Fig. 6. The partition model of phosphorus between solid metal and liquid metal varies with pressure. (a) The measured D_P in the Fe—S—P ternary system from this study at 3 and 5 GPa. (b) The partition coefficient of phosphorus between the liquid and solid metal lgD$_P$, is plotted with our estimated partition model. (c) Comparison between calculated and measured values of lgD_P. All the data are from this study and previous studies on the Fe-Ni—S—P system. Solid line is a 1:1 identify line plotted for reference. SS07: Stewart and Schmidt (2007); S09: Stewart et al. (2009).

5. IMPLICATION FOR THE LUNAR CORE

5.1. Constraints on the (S + P) in the lunar core

Antonangeli et al. (2015) proposed a velocity and density model for the lunar core, and that the liquid outer core mass is 49 % of the total core mass. In the following discussions, we used the same core mass model as Antonangeli et al. (2015) to calculate the sulfur and phosphorus concentrations in the lunar core. We then used a core mass balance model:

$$C^i_{core} = (1-x)C^i_{ic} + xC^i_{oc} \quad (4)$$

where x is the mass fraction of the lunar outer core, and C^i_{core}, C^i_{ic} and C^i_{oc} are the concentrations of element i in the lunar core, lunar inner core and lunar outer core, respectively. Our experimental results show that near none of the sulfur is in the solid inner core, suggesting the value of C^S_{oc} is almost twice of the C^S_{core}. This basic assumption is key throughout the following discussion.

The sulfur and phosphorus abundances in the lunar core are highly associated with the melting temperature at the lunar core-mantle boundary (CMB). The CMB temperature would be constrained between 1603 K and 1743 K (Mallik et al., 2019; Weber et al., 2011). The ICB temperature may be only a few tens of kelvins higher than that at CMB because the lunar liquid core is subadiabatic (Weber et al., 2011). Assuming the temperature at ICB is 1650–1800 K, then the amount of (S + P) in the liquid phase could range from 8.7 to 13.1 wt% (corresponding to 4.3–6.4 wt% in the bulk lunar core) (Fig. 7a).

As the core cools in the future Moon, the CMB temperature to a low temperature (e.g., 1300 K), and the mass of the liquid outer core becomes small. Due to the lower solubility of S and P in solid Fe, a small liquid outer core may be sulfur-rich, making an Fe-S liquid layer and an Fe-P liquid layer because of immiscibility melts in Fe—S—P system.

As listed in Table S1, the sulfur solubility in crystalline iron is approximately 0.05 wt% at 5 GPa, and the sulfur abundance in the solid inner core can be simply estimated

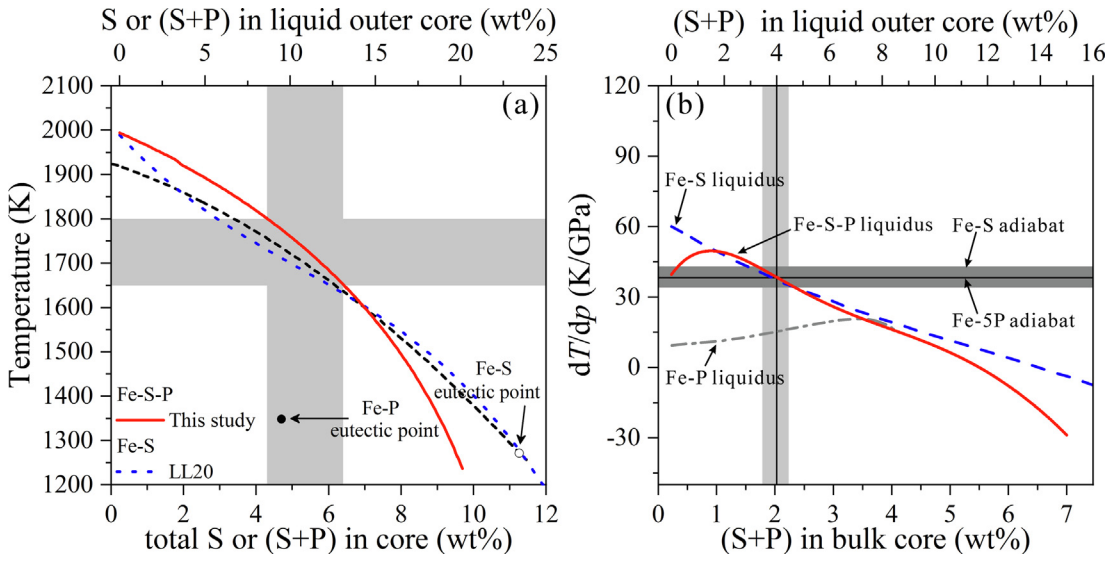

Fig. 7. Constraints on the (S + P) content in the lunar core and liquidus and adiabatic temperature gradient and freezing regimes of the lunar core. (a) The tradeoff between the total abundance of (S + P) in the lunar core and the temperatures. The black dot-dashed line is the liquidus curve of lunar core reported by Weber et al. (2011). The open and solid circle are the eutectic point of Fe-S at 5.1 GPa (Liu and Li, 2020) and Fe-P system at 6 GPa (Minin et al., 2019), respectively. (b) Three curves represent the pressure dependence of the liquidus in the Fe-S binary system (Liu and Li, 2020), Fe-P binary system (Chantel et al., 2018), and Fe—S—P ternary system. The horizon shade region represents the adiabatic temperature gradient of 34–43 K/GPa in an Fe-S lunar core (Williams, 2009; Jing et al., 2014) and the horizon black line represents the adiabatic temperature gradient of 38.1 K/GPa of Fe-5 wt% P, which interpolates from the Fe and $Fe_{75}P_{25}$ alloys. LL20: Liu and Li (2020); W11: Weber et al. (2011).

as 0.05 wt%. For an S—P—bearing lunar core, the value of lgD_P is near −0.88 (corresponding to a D_P of ∼ 0.13, Fig. 6a). When ∼ 0.3 wt% phosphorus is in the lunar core (Yin et al., 2019) and the liquid outer core is 49 % of the total core mass, the phosphorus abundance in the solid inner core and liquid outer core is estimated to be 0.07 ± 0.01 wt% and 0.54 ± 0.01 wt%, respectively. Therefore, the abundance of phosphorus and sulfur in the solid inner core would be nearly equal and very low. To date, the most justified lunar core mass model suggests a solid iron inner core with a radius of 134–203 km and a density of 7.6–7.8 g/cm^3, and a liquid Fe-S outer core with a radius of 265–381 km and a density of 5.7–6.3 g/cm^3 (Antonangeli et al., 2015; Matsuyama et al., 2016). Due to the similar molar mass of sulfur and phosphorus, we assumed that the effect of 0.05 wt% sulfur and 0.07 wt% phosphorus on the density of the inner core is equal to that of 0.12 wt% sulfur. According to the reported the temperature dependence of the density of Fe-S solutions at 5 GPa by Kuskov and Belashchenko (2016), we estimated the density of an Fe—S—P (0.05 wt% S and 0.07 wt% P) inner core to be 7.72 g/cm^3 by linear fitting of the sulfur content and the theoretically determined Fe-S density relationship (0 at.% S: 1500 K, 7.87 g/cm^3; 1800 K, 7.47 g/cm^3; 6 at.% S: 1500 K, 7.23 g/cm^3; 1800 K, 7.08 g/cm^3, Kuskov and Belashchenko, 2016) at 5 GPa and 1600 K.

According to the measured partition coefficient value of phosphorus (D_P of ∼ 0.13) at 5 GPa in this study, the mole fraction of sulfur in the liquid metal is approximately 10–12 mol% by Eq. (3), indicating a sulfur content of 6.08–7.15 wt% in the liquid outer core. This value agrees well with previous studies (6–8 wt%, Rai and van Westrenen, 2014; Steenstra et al., 2016; 10.7–14.4 wt% in the outer core, Weber et al., 2011; 3–6 wt%, Antonangeli et al., 2015; Jing et al., 2014; 2–4 wt%, Liu and Li, 2020). Relying on our estimation of 0.54 ± 0.01 wt% phosphorus in the liquid outer core, the summed (S + P) content in the outer core is thus about 6.61–7.68 wt%. In this case, the density of the Fe—S—P lunar outer core could be near 5.94–6.09 g/cm^3, according to the density model of Fe-S liquids at 5 GPa by Jing et al. (2014). In summary, an Fe—S—P lunar core may contain 0.07 wt% P and 0.05 wt% S in the solid inner core, and 0.54 wt% P and 6.08–7.05 wt% S in the liquid outer core.

Nickel is also a potential major alloying element in the lunar core, assuming that the lower limit of the estimated Fe/Ni ratio in the bulk Moon corresponds to a chondritic Fe/Ni ratio of 17 (Lodders and Fegley, 1998). The partition coefficient values of the phosphorus and sulfur mole fractions in the melt could be inferred from our partition model to be 0.13 ± 0.03 and 10–12 mol%, respectively, for an Fe-Ni—S—P lunar core model. The solubility of phosphorus in metallic iron in the Fe-P system (Minin et al., 2019) and Fe-Ni-P system (Minin et al., 2018) at 6 GPa is about 2.8 wt%, which means nickel could not increase the solubility of phosphorus in solid iron. Therefore, our phosphorus partition model estimates the sulfur concentration to be<11.4 ± 0.1 wt% when the liquid lunar core has a maximum Ni content of 4.9 wt%. As an upper limit of sulfur content in the liquid outer core, our Ni-free result (6.08–7.05 wt% S) in the Fe—S—P system is within this range.

5.2. Solidification scheme of the lunar inner core

A convecting metallic liquid core is one of the criteria for a planetary body to generate and sustain a global magnetic dipole (Evans et al., 2018). The compositional buoyancy from the exsolution of the light elements (e.g., Si, S, O, and C) at an inner core boundary is one of the driving forces of such fluid motion (Buffett et al., 2000). Assuming that the lunar core is well mixed, its thermal profile would follow the adiabatic gradient $\frac{dT}{dp}$, as a relation of.

$$\frac{dT}{dp} = \frac{\alpha T}{\rho C_P} = \left(\frac{\alpha_0 T_0}{\rho_0 C_{P0}}\right)\left(\frac{\rho_0}{\rho}\right)^{\delta_S+1} \quad (5)$$

where α, ρ and C_P are the thermal expansion coefficient, density and heat capacity at relevant pressure and temperatures, respectively. α_0, ρ_0 and C_{P0} are the corresponding parameters at 1 bar, and δ_S is the adiabatic Anderson-Grüneisen parameter. As shown in Fig. 7b, the pressure dependence of liquidus temperature $\frac{dT}{dp}$ of the Fe-S system crosses the adiabatic temperature gradient (34–43 K/GPa, Jing et al., 2014; Williams, 2009) near 4.0 ± 0.3 wt% (Fig. 7b), and a transition of the inner core solidification mechanism may thus have happened during lunar history in this situation (Liu and Li, 2020). Without Fe-P liquid adiabat temperature gradient data, Chantel et al. (2018) compared the pressure dependence of Fe-P liquidus temperature with the adiabat temperature gradient of Fe and Fe-5 wt% S and implied that a phosphorus-poor metallic core would initially freeze from the top, while a phosphorus-rich core would solidify from the bottom. Later, Kinoshita et al. (2020) constructed an adiabatic Murnaghan equation of state for liquid $Fe_{75}P_{25}$ as a function of potential temperature at 1 bar. Thus, the density ρ_0 and the thermal expansion α_0 could be estimated as 6.18 g/cm^3 and 9.24–9.27 × 10^{-5} K^{-1} at a potential temperature of 1673 K at 1 bar, respectively. The density of liquid $Fe_{75}P_{25}$ under ICB conditions is about 6.48–6.52 g/cm^3. Using $\delta_S \sim 1$ and C_{P0} of 835 J kg^{-1} K^{-1} (Desai, 1986), the estimated adiabatic temperature gradient is ~ 26.8 ± 0.5 K/GPa for a liquid $Fe_{75}P_{25}$ alloy (Fig. 7b) by Eq. (5). It is worth noting that the lunar core cannot contain so much phosphorus, and that the relative phosphorus-poor (Fe-5 wt% P or Fe-10 wt% P) adiabat temperature gradient is more reasonable to be used as a normative value. We estimate an adiabat temperature gradient of ~ 38.2 K/GPa for Fe-5 wt% P (Fe-5P) melts, calculated by a linear interpolation from Fe (41 K/GPa, Williams, 2009) and the $Fe_{75}P_{25}$ alloy.

Secular cooling of planetary bodies ultimately brings the core to a temperature at which macroscopic solid metal is thermodynamically stable (Nimmo, 2015). The growth rate of an Earth-like inner core depends on the liquidus with pressure (Nimmo, 2009) which can be determined from the liquidus curve of core composition under different pressures. The four sets of inconsistent liquidus temperature gradient mainly due to the pressure effect on the liquidus curve of core composition (Liu and Li, 2020). As shown in Fig. 7b, the pressure dependence of the Fe—S—P liquidus curve flips slightly from positive when the (S + P) content is < ~1.4 wt% to negative when the (S + P) content is > ~1.4 wt% in the outer core. The pressure dependence of Fe—S—P liquidus temperature crosses the Fe-S adiabat temperature gradient at 3.5–4.5 wt% (S + P) (shaded regions in Fig. 7b) and crosses the Fe-5P adiabat temperature gradient at 4.3 wt% (S + P).

In applying this result to planetary core solidification (Fig. 8), if the (S + P) content in the primordial liquid bulk core $(S+P)_{bc}$ is < 1.7 wt% (corresponding to $(S+P)_{oc}$ < 3.5-wt% by the mass balance model from Antonangeli et al., 2015), the pressure dependence of the Fe—S—P liquidus temperature $(dT/dp)_{liq}$ is greater than that of the Fe-Sand Fe-5P adiabats $(dT/dp)_{ad}$. On this occasion, iron will crystallize to an inner core nucleus, and the core will freeze from the inside out upon further cooling (Fig. 8a). Meanwhile, phosphorus may have a greater impact on the solidification rate of the inner core than sulfur because of the positive trend of the pressure dependence curve on the Fe—S—P liquidus when the (S + P) content is less than 1.4 wt% (Fig. 7b). If the (S + P) content in the primordial liquid bulk core $(S + P)_{bc}$ is > 4.5 wt% (corresponding to $(S+P)_{oc}$ >9.18 wt%), the pressure-dependence of $(dT/dp)_{liq}$ is considerably below those of the Fe-S and Fe-5P adiabats $(dT/dp)_{ad}$. In this case, iron will precipitate at the CMB and may fall as iron snow, resulting in a snowing scenario (Fig. 8c). If the $(S + P)_{bc}$ is between 1.7 wt% and 4.5 wt% (corresponding to $(S + P)_{oc}$ of 3.4–9.2 wt%), the core solidification mechanism will transfer from a bottom-up to a top-down regime as the core cools during lunar evolution (Fig. 8b).

According to the phase diagram in Fig. 3, such a low (S + P) content would yield a miscible liquid metal, indicating a primordial homogeneous molten lunar core (~2200 K, Rai and van Westrenen, 2014). Our model (an outer core with 0.54 wt% P and 6.08–7.05 wt% S), would result in initial 0.3 wt% phosphorus and 2.98–3.45 wt% sulfur budget in the lunar core, respectively. Our sulfur budget in the primordial lunar core is lower than the estimation (6 wt%) from the core-mantle differentiation model by Rai and van Westrenen (2014) but agrees with the study by Righter et al., (2017). Our new models on the abundances of phosphorus and sulfur in the lunar core are more aligned with the above mentioned third solidification regime (Fig. 8b). As the core solidifies from the bottom-up, the liquid outer core becomes S- and P-rich until the inner core and outer core reach equilibrium. When the (S + P) content in the outer core is more than 3.5 wt%, the solidification regime will switch from bottom-up to top-down (Fig. 8b), causing iron to precipitate in the form of "snow" on top of the core, which is likely a common core crystallization scenario in small bodies in the solar system (Williams, 2009).

6. CONCLUSION

We experimentally determined the phase diagram of the Fe—S—P ternary system on the iron-rich side under pressures of 3 and 5 GPa and temperatures of 1173–1873 K. The phosphorus partition coefficient between solid metal

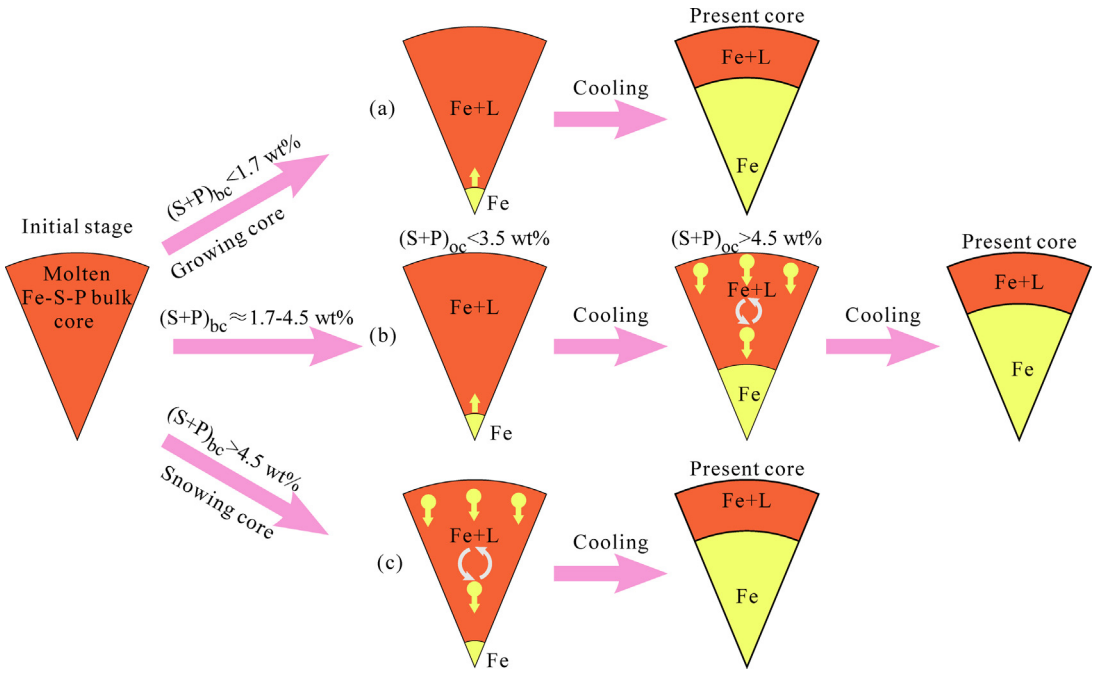

Fig. 8. Evolutionary scenarios of the cooling Fe—S—P lunar core. The crystallization regimes for the inner core depend on the (S + P) content in the initial fully molten bulk core $(S + P)_{bc}$. (a): The bottom-up regime. If $(S + P)_{bc} < 1.7$ wt%, the inner core grows from the bottom. (b): The bottom-up regime transforms to the top-down regime. If $(S + P)_{bc}$ between 1.7 wt% and 3.5 wt%, the solidification mechanism transforms from the bottom-up regime to the top-down regime. (c): The top-down regime. If $(S + P)_{bc}$ greater than 4.5 wt%, iron precipitates in the form of "snow" on top of the core.

and liquid metal is significantly associated with the sulfur content in the melts. The value of the phosphorus partition coefficient increases with increasing pressure. Moreover, the tradeoff between the lunar CMB temperature and the liquidus curve of the Fe—S—P system constrains the concentration of (S + P) in the lunar outer core to be < 10.17–12.24 wt% (equivalent to 5.4–6.2 wt% in bulk core). In a complex composition model (Fe-Ni—S—P) for the lunar core, the sulfur abundance is estimated to be < 11.4 ± 0.1 wt% in the outer core according to the partitioning of sulfur in the core. Assuming that the phosphorus content of the lunar bulk core is ~ 0.3 wt%, the phosphorus concentration is estimated to be 0.07 ± 0.01 wt% in the solid inner core and 0.54 ± 0.01 wt% in the liquid outer core. We also estimated the sulfur content to be 0.05 ± 0.01 wt% in the inner core and 6.08–7.15 wt% in the outer core, depending upon the sulfur solubility in the solid iron and our phosphorus partitioning model. The miscible liquid observed in this study predicts a lower limit of the boundary between the one liquid field and two liquid fields in the Fe—S—P ternary system under high-pressure conditions and further indicates a fully molten, homogenous initial lunar core (~2200 K, Rai and van Westrenen, 2014). Integrating the liquidus curve of the Fe—S—P system obtained in this study and the adiabatic temperature gradient of the Fe-S and Fe-P (phosphorus-poor) core models from previous studies, the solidification regime of the lunar inner core is predicted to switch from the bottom-up to the up-down regime once the (S + P) content in the lunar outer core exceeded 3.5 wt% during lunar evolution.

DECLARATION OF COMPETING INTEREST

The authors declare that they have no known competing financial interests or personal relationships that could have appeared to influence the work reported in this paper.

ACKNOWLEDGMENTS

The authors thank B. Mo for her help on SEM analysis and X. Li for his help of EPMA analysis. We acknowledge Dr. Joshua Muir for his help to improve the writing. This work was financially supported by the National Natural Science Foundation of China (Grant No. 41873073), the Strategic Priority Research Program of Chinese Academy of Sciences (Grant No. XDB 41000000), and the International Partnership Program of Chinese Academy of Sciences (Grant No. 132852KYSB20200011).

APPENDIX A. SUPPLEMENTARY MATERIAL

Supplementary material to this article can be found online at https://doi.org/10.1016/j.gca.2022.07.024.

REFERENCES

Antonangeli D., Morard G., Schmerr N. C., Komabayashi T., Krisch M., Fiquet G. and Fei Y. (2015) Toward a mineral physics reference model for the Moon's core. *Proc. Natl. Acad. Sci.* **112**, 3916–3919.

Bean V. E., Akimoto S., Bell P. M., Block S., Holzapfel W. B., Manghnani M. H., Nicol M. F. and Stishov S. M. (1986)

Another step toward an international practical pressure scale: 2nd AIRAPT IPPS task group report. *Physica.* **139**, 52–54.
Bohlen S. R. and Boettcher A. L. (1982) The quartz-coesite transformation: A precise determination and the effects of other components. *J. Geophys. Res.* **87**, 7073–7078.
Brett R. and Bell P. M. (1969) Melting relations in the Fe-rich portion of the system Fe-FeS at 30 kb pressure. *Earth Planet. Sci. Lett.* **6**, 479–482.
Buffett B. A., Garnero E. J. and Jeanloz R. (2000) Sediments at the top of Earth's core. *Science* **290**, 1338–1342.
Buono A. S. and Walker D. (2011) The Fe-rich liquidus in the Fe-FeS system from 1 bar to 10 GPa. *Geochim. Cosmochim. Acta* **75**, 2072–2087.
Chabot N. L. and Drake M. J. (2000) Crystallization of magmatic iron meteorites: The effects of phosphorus and liquid immiscibility. *Meteorit. Planet. Sci.* **35**, 807–816.
Chacko S. and De Bremaecker J. C. (1982) The evolution of the moon: A finite element approach. *Moon Planets* **27**, 467–492.
Chantel J., Jing Z., Xu M., Yu T. and Wang Y. (2018) Pressure dependence of the liquidus and solidus temperatures in the Fe-P binary system determined by in situ ultrasonics: Implications to the solidification of Fe-P liquids in planetary cores. *J. Geophys. Res. Planets* **123**, 1113–1124.
Corgne A., Wood B. J. and Fei Y. (2008) C-and S-rich molten alloy immiscibility and core formation of planetesimals. *Geochim. Cosmochim. Acta* **72**, 2409–2416.
Dasgupta R., Buono A., Whelan G. and Walker D. (2009) High-pressure melting relations in Fe–C–S systems: Implications for formation, evolution, and structure of metallic cores in planetary bodies. *Geochim. Cosmochim. Acta* **73**, 6678–6691.
Deng L., Fei Y., Liu X., Gong Z. and Shahar A. (2013) Effect of carbon, sulfur and silicon on iron melting at high pressure: Implications for composition and evolution of the planetary terrestrial cores. *Geochim. Cosmochim. Acta* **114**, 220–233.
Desai P. D. (1986) Thermodynamic properties of iron and silicon. *J. Phys. Chem. Ref. Data* **15**, 967–983.
Ding S., Hough T. and Dasgupta R. (2018) New high pressure experiments on sulfide saturation of high-FeO^* basalts with variable TiO_2 contents–Implications for the sulfur inventory of the lunar interior. *Geochim. Cosmochim. Acta* **222**, 319–339.
Evans A. J., Tikoo S. M. and Andrews-Hanna J. C. (2018) The case against an early lunar core dynamo powered by core convection. *Geophys. Res. Lett.* **45**, 98–107.
Fei Y., Bertka C. M. and Finger L. W. (1997) High-pressure iron-sulfur compound, Fe_3S_2, and melting relations in the Fe-FeS system. *Science* **275**, 1621–1623.
Fei Y. and Brosh E. (2014) Experimental study and thermodynamic calculations of phase relations in the Fe-C system at high pressure. *Earth Planet. Sci. Lett.* **408**, 155–162.
Fei Y., Li J., Bertka C. M. and Prewitt C. T. (2000) Structure type and bulk modulus of Fe_3S, a new iron–sulfur compound. *Am. Mineral.* **85**, 1830–1833.
Garcia R. F., Gagnepain-Beyneix J., Chevrot S. and Lognonné P. (2011) Very preliminary reference Moon model. *Phys. Earth Planet. Inter.* **188**, 96–113.
Hayden L. A., Van Orman J. A., McDonough W. F., Ash R. D. and Goodrich C. A. (2011) Trace element partitioning in the Fe-S-C system and its implications for planetary differentiation and the thermal history of ureilites. *Geochim. Cosmochim. Acta* **75**, 6570–6583.
Hirayama Y., Fujii T. and Kurita K. (1993) The melting relation of the system, iron and carbon at high pressure and its bearing on the early stage of the Earth. *Geophys. Res. Lett.* **20**, 2095–2098.
Jing Z., Wang Y., Kono Y., Yu T., Sakamaki T., Park C., Rivers M. L., Sutton S. R. and Shen G. (2014) Sound velocity of Fe-S liquids at high pressure: implications for the Moon's molten outer core. *Earth Planet. Sci. Lett.* **396**, 78–87.
Jones J. H. and Drake M. J. (1983) Experimental investigations of trace element fractionation in iron meteorites, II: The influence of sulfur. *Geochim. Cosmochim. Acta* **47**, 1199–1209.
Jones J. H. and Malvin D. J. (1990) A nonmetal interaction model for the segregation of trace metals during solidification of Fe-Ni-S, Fe-Ni-P, and Fe-Ni-S-P alloys. *Metall. Trans. B* **21**, 697–706.
Kinoshita D., Nakajima Y., Kuwayama Y., Hirose K., Iwamoto A., Ishikawa D. and Baron A. Q. R. (2020) Sound Velocity of Liquid Fe-P at High Pressure. *Phys. Status Solidi B* **257**, 2000171.
Kuskov O. L. and Belashchenko D. K. (2016) Thermodynamic properties of Fe-S alloys from molecular dynamics modeling: Implications for the lunar fluid core. *Phys. Earth Planet. Inter.* **258**, 43–50.
Kuskov O. L. and Kronrod V. A. (1998) Constitution of the Moon 5. Constraints on composition, density, temperature, and radius of a core. *Phys. Earth Planet. Inter.* **107**, 285–306.
Kuskov O. L., Kronrod E. V. and Kronrod V. A. (2019) Effect of thermal state on the mantle composition and core sizes of the Moon. *Geochem. Int.* **57**, 605–620.
Lai X., Zhu F., Liu Y., Bi W., Zhao J., Alp E. E., Hu M. Y., Zhang D., Tkachev S., Manghnani M. H., Prakapenka V. B. and Chen B. (2020) Elastic and magnetic properties of Fe_3P up to core pressures: Phosphorus in the Earth's core. *Earth Planet. Sci. Lett.* **531** 115974.
Laneuville M., Wieczorek M. A., Breuer D. and Tosi N. (2013) Asymmetric thermal evolution of the Moon. *J. Geophys. Res. Planets* **118**, 1435–1452.
Laneuville M., Wieczorek M. A., Breuer D., Aubert J., Morard G. and Rückriemen T. (2014) A long-lived lunar dynamo powered by core crystallization. *Earth Planet. Sci. Lett.* **401**, 251–260.
Li J. and Fei Y. (2014) Experimental constraints on core composition. In *Treatise on Geochemistry* (ed. R. W. Carlson). Elsevier, New York, pp. 527–557.
Li J., Fei Y., Mao H. K., Hirose K. and Shieh S. R. (2001) Sulfur in the Earth's inner core. *Earth Planet. Sci. Lett.* **193**, 509–514.
Liu L. G. and Bassett W. A. (1975) The melting of iron up to 200 kbar. *J. Geophys. Res.* **80**, 3777–3782.
Liu J. and Li J. (2020) Solidification of lunar core from melting experiments on the Fe-Ni-S system. *Earth Planet. Sci. Lett.* **530**, 1–9.
Lodders K. and Fegley B. (1998) *The planetary scientist's companion*. Oxford University Press, New York.
Mallik A., Ejaz T., Shcheka S. and Garapic G. (2019) A petrologic study on the effect of mantle overturn: Implications for evolution of the lunar interior. *Geochim. Cosmochim. Acta* **250**, 238–250.
Malvin D. J., Jones J. H. and Drake M. J. (1986) Experimental investigations of trace element fractionation in iron meteorites. III: Elemental partitioning in the system Fe-Ni-S-P. *Geochem. Cosmochim. Acta* **50**, 1221–1231.
Matsuyama I., Nimmo F., Keane J. T., Chan N. H., Taylor G. J., Wieczorek M. A., Kiefer W. S. and Williams J. G. (2016) GRAIL, LLR, and LOLA constraints on the interior structure of the Moon. *Geophys. Res. Lett.* **43**, 8365–8375.
Mighani S., Wang H., Shuster D. L., Borlina C. S., Nichols C. O. and Weiss B. P. (2020) The end of the lunar dynamo. *Sci. Adv.* **6**, eaax0883.
Minin, D.A., Shatskiy, A., Litasov, K.D., 2018. Fe–Ni–P phase diagram at 6 GPa. *81st An. Met. Soc.* Lunar Planet. Inst., Moscow. #2067(abstr.).

Minin D. A., Shatskiy A. F., Litasov K. D. and Ohfuji H. (2019) The Fe-Fe_2P phase diagram at 6 GPa. *High Pressure Res.* **39**, 50–68.

Morard G. and Katsura T. (2010) Pressure-temperature cartography of Fe-S-Si immiscible system. *Geochim. Cosmochim. Acta* **74**, 3659–3667.

Nimmo F. (2009) Energetics of asteroid dynamos and the role of compositional convection. *Geophys. Res. Lett.* **36**, L10201.

Nimmo F. (2015) *Energetics of the core*. Elsevier, pp. 27–55.

O'Neill H. S. C. (1991) The origin of the moon and the early history of the earth-a chemical model, part 2: the earth. *Geochim. Cosmochim. Acta* **55**, 1159–1172.

Pommier A. (2018) Influence of sulfur on the electrical resistivity of a crystallizing core in small terrestrial bodies. *Earth Planet. Sci. Lett.* **496**, 37–46.

Raghavan V. (1988) *Phase Diagrams of Ternary Iron Alloys. Part 2: Ternary Systems Containing Iron and Sulphur*. Indian Institute of Metals, Calcutta.

Rai N. and van Westrenen W. (2014) Lunar core formation: new constraints from metal-silicate partitioning of siderophile elements. *Earth Planet. Sci. Lett.* **388**, 343–352.

Righter K. (2002) Does the Moon have a metallic core? Constraints from giant impact modeling and siderophile elements. *Icarus* **158**, 1–13.

Righter K. (2019) Volatile element depletion of the moon-the roles of precursors, post-impact disk dynamics, and core formation. *Sci. Adv.* **5**, 1–8.

Righter K. and Drake M. J. (1996) Core formation in Earth's Moon, Mars, and Vesta. *Icarus* **124**, 513–529.

Righter K. and Drake M. J. (2000) Metal/silicate equilibrium in the early Earth-New constraints from the volatile moderately siderophile elements Ga, Cu, P, and Sn. *Geochem. Cosmochim. Acta* **64**, 3581–3597.

Righter K., Go B. M., Pando K. A., Danielson L., Ross D. K., Rahman Z. and Keller L. P. (2017) Phase equilibria of a low S and C lunar core: Implications for an early lunar dynamo and physical state of the current core. *Earth Planet. Sci. Lett.* **463**, 323–332.

Sahajwalla V. and Khanna R. (2003) Effect of sulfur on the dissolution behavior of graphite in Fe-C-S melts: A Monte Carlo simulation study. *Scand. J. Metall.* **32**, 53–57.

Scott H. P., Huggins S., Frank M. R., Maglio S. J., Martin C. D., Meng Y., Santillán J. and Williams Q. (2007) Equation of state and high-pressure stability of Fe_3P-schreibersite: Implications for phosphorus storage in planetary cores. *Geophys. Res. Lett.* **34**, L06302.

Shan S., Wang R., Guo J. and Li H. (2007) Pressure calibration for the sample cell of YJ-3000t multianvil press at high-temperature and high-pressure. *Chin. J. High Press. Phys.* **21**, 367–372.

Siebert J., Guyot F. and Malavergne V. (2005) Diamond formation in metal-carbonate interactions. *Earth Planet. Sci. Lett.* **229**, 205–216.

Steenstra E. S., Rai N., Knibbe J. S., Lin Y. H. and van Westrenen W. (2016) New geochemical models of core formation in the Moon from the metal–silicate partitioning of 15 siderophile elements. *Earth Planet. Sci. Lett.* **441**, 1–9.

Steenstra E. S., Lin Y. H., Rai N., Jansen M. and van Westrenen W. (2017a) Carbon as the dominant light element in the lunar core. *Am. Mineral.* **102**, 92–97.

Steenstra E. S., Sitabi A. B., Lin Y. H., Rai N., Knibbe J. S., Berndt J., Matveev S. and van Westrenen W. (2017b) The effect of melt composition on metal-silicate partitioning of siderophile elements and constraints on core formation in the angrite parent body. *Geochim. Cosmochim. Acta* **212**, 62–83.

Stewart A. J. and Schmidt M. W. (2007) Sulfur and phosphorus in the Earth's core: The Fe-P-S system at 23 GPa. *Geophys. Res. Lett.* **34**, L13201.

Stewart A. J., van Westrenen W., Schmidt M. W. and Günther D. (2009) Minor element partitioning between fcc Fe metal and Fe-S liquid at high pressure: the role of crystal lattice strain. *Earth Planet. Sci. Lett.* **284**, 302–309.

Tao R. and Fei Y. (2021) High-pressure experimental constraints of partitioning behavior of Si and S at the Mercury's inner core boundary. *Earth Planet. Sci. Lett.* **562** 116849.

Teplyakova S. N. (2011) Evolution of molten material in iron cores of small planets. *Solar Syst. Res.* **45**, 515–522.

Wade J. and Wood B. J. (2005) Core formation and the oxidation state of the Earth. *Earth Planet. Sci. Lett.* **236**, 78–95.

Wang C., Hirama J., Nagasaka T. and Banya S. (1991) Phase equilibria of liquid Fe-S-C ternary system. *ISIJ Int.* **31**, 1292–1299.

Weber R. C., Lin P. Y., Garnero E. J., Williams Q. and Lognonné P. (2011) Seismic detection of the Lunar core. *Science* **331**, 309–312.

Williams Q. (2009) Bottom-up versus top-down solidification of the cores of small solar system bodies: constraints on paradoxical cores. *Earth Planet. Sci. Lett.* **284**, 564–569.

Yin Y., Li Z. and Zhai S. (2019) The phase diagram of the Fe-P binary system at 3 GPa and implications for phosphorus in the lunar core. *Geochim. Cosmochim. Acta* **254**, 54–66.

Yin Y., Wang L., Zhai S. and Fei Y. (2022) Electrical resistivity of Fe and Fe-3 wt% P at 5 GPa with implications for the Moon's core conductivity and dynamo. *J. Geophys. Res. Planets* **127**, e2021JE007116.

Zaitsev A. I., Dobrokhotova Z. V., Litvina A. D. and Mogutnov B. M. (1995) Thermodynamic properties and phase equilibria in the Fe-P system. *J. Chem. Soc. Faraday Trans.* **91**, 703–712.

Zhang B., Ge J., Xiong Z. and Zhai S. (2019) Effect of water on the thermal properties of olivine with implications for lunar internal temperature. *J. Geophys. Res. Planets* **124**, 3469–3481.

Zhang N., Parmentier E. M. and Liang Y. (2013) A 3D numerical study of the thermal evolution of the Moon after cumulate mantle overturn: the importance of rheology and core solidification. *J. Geophys. Res. Planets* **118**, 1789–1804.

Associate editor: Rajdeep Dasgupta